Partial correlation-based functional connectivity analysis for functional near-infrared spectroscopy signals

Ata Akın

Partial correlation-based functional connectivity analysis for functional near-infrared spectroscopy signals

Ata Akın*
Acibadem University, Department of Medical Engineering, Atasehir, Istanbul, Turkey

Abstract. A theoretical framework, a partial correlation-based functional connectivity (PC-FC) analysis to functional near-infrared spectroscopy (fNIRS) data, is proposed. This is based on generating a common background signal from a high passed version of fNIRS data averaged over all channels as the regressor in computing the PC between pairs of channels. This approach has been employed to real data collected during a Stroop task. The results show a strong significance in the global efficiency (GE) metric computed by the PC-FC analysis for neutral, congruent, and incongruent stimuli (NS, CS, IcS; $GE_N = 0.10 \pm 0.009$, $GE_C = 0.11 \pm 0.01$, $GE_{IC} = 0.13 \pm 0.015$, $p = 0.0073$). A positive correlation ($r = 0.729$ and $p = 0.0259$) is observed between the interference of reaction times (incongruent–neutral) and interference of GE values ($GE_{IC} - GE_N$) computed from [HbO] signals. © *2017 Society of Photo-Optical Instrumentation Engineers (SPIE)* [DOI: 10.1117/1.JBO.22.12.126003]

1 Introduction

The main challenge of the state-of-art of functional near-infrared spectroscopy (fNIRS) systems has been to accurately recover the deep cortical signals that are undoubtedly buried inside the upper layer hemodynamic signals. Since the measurements are performed from the skin surface, the photons travelling from a source to a detector will be modulated by the hemodynamic changes occurring at each layer. fNIRS techniques have been shown to suffer from the corruption of upper layer hemodynamic activity and only a fraction of the signal measured is attributed to cortical signals.[1] The source–detector configuration necessary to ensure a penetration to the cortical level results in unfortunate sampling from the skin, where systemic physiological changes are reflected as hemodynamic changes. Hence, any further analysis on these signals will suffer from the corruption of these systemic fluctuations.[2–10] One major analysis, where this corruption will lead to false positives, is the functional connectivity (FC) studies.

FC can be computed most easily by the use of a correlation coefficient between channels of fNIRS measurements. For a multichannel system, the correlation coefficient $\hat{\rho}_{ij}$ between any two channels (x_i and x_j) can be computed by

$$\hat{\rho}_{ij} = \frac{C(x_i, x_j)}{\sigma_{x_i} \sigma_{x_j}}, \tag{1}$$

where $C(x_i, x_j)$ is the covariance between the two channels, σ_{x_i} and σ_{x_j} are the standard deviations of the variables x_i and x_j. Due to physics of photon propagation in turbid media, the collected signal will be carrying information from the underlying tissues. Hence the signal, x_i, will include cortical as well as noncerebral tissue dynamics. The collected signal can then be modeled as a weighted sum of the activities of the underlying tissues:

$$x_i(t) = w_b s_i^b(t) + w_s s^s(t) + n(t), \tag{2}$$

where w_b and w_s are the contributions (i.e., percentage) of a signal [i.e., the regional brain signal, s_i^b, the systemic signal, $s^s(t)$] to the signal at the channel, and $n(t)$ is the instrumentation and other random noises modeled as a Gaussian zero mean white process. Hence, by substituting Eq. (2) into Eq. (1), combining $s^{sn} = s^s(t) + n(t)$, and expanding the nominator and denominator terms, we get

$$\hat{\rho}_{ij} = \frac{C(s_i^b, s_j^b) + C(s_i^b, s^{sn}) + C(s_j^b, s^{sn}) + C(s^{sn}, s^{sn})}{\sqrt{\sigma^2(s_i^b) + \sigma^2(s^{sn}) + 2C(s_i^b, s^{sn})}\sqrt{\sigma^2(s_j^b) + \sigma^2(s^{sn}) + 2C(s_j^b, s^{sn})}}, \tag{3}$$

but we are interested only in finding the correlation between the cortical regions:

$$\rho_{ij} = \frac{C(s_i^b, s_j^b)}{\sigma_{s_i^b} \sigma_{s_j^b}}. \tag{4}$$

*Address all correspondence to: Ata Akin, E-mail: ata.akin@acibadem.edu.tr

Since we do not have access to the individual covariances and variances in Eq. (3), we need to propose a method to extract this information. The issue, then, becomes the proper and accurate way of regressing out the contaminating signals to estimate the correlation of the brain regions, as the definition of FC requires. Several researchers have proposed to use a second detector placed closer to the source (short separation detector) that will be sensitive to changes only on the superficial layers to regress out the systemic fluctuations contaminating a detector placed farther away from the source.[2,6,9–15] The use of an SSD has been investigated deeply due to its ambiguity of its placement (how short is short enough?).[11] It also increases instrumentation and data analysis complexity, not to mention the extra burden it brings to ergonomics of the probe. Hence, many have promoted the use of advanced signal processing techniques to overcome the contamination problem. This paper is yet another proposal that advocates the use of such a technique to maintain the view that "few is better."

We propose the use of a partial correlation (PC)-based FC analysis that removes the unwanted correlation due to extracerebral contamination. In many of fMRI and fNIRS studies, PC is considered as a suitable criterion for investigation and understanding of brain FC.[16–23] FC studies using fNIRS have been conducted recently[17,24–31] and have further been linked to graph theoretical approaches.[32] Similarly, FC analysis with the PC approach has been proposed both by our group and others.[17,23,33,34] Our group has shown that using the remaining 14 channels of a 16-channel fNIRS measurement system as the regressors of the PC analysis, we can provide reliable estimate of the FC analysis. The assumption behind this approach was that there are local systemic fluctuations at each measurement site (channel) and they are also picked up by any channel. Hence, when computing the correlation between two channels, one must take into account the distorting affect of the remaining 14 channels. This paper challenges this assumption by the fact that there is one unique systemic fluctuation embedded in each channel, and that its frequency content is different from the hemodynamic response to cognitive stimulus. This systemic fluctuation can be recovered by taking an average of the high pass filtering of the signal from each channel. Hence, our aim in this paper is to propose a theoretical framework to compute the FC of fNIRS signals based on the PC approach and a signal processing algorithm that can be adopted in computing the FC for fNIRS data.

2 Methods

The first part of Sec. 2 presents a simulation study that generates synthetic data to investigate if PC-based connectivity outperforms the conventional correlation analysis for computing FC-derived metrics. The second part of the section explains how the multichannel fNIRS data have been processed to provide PC-based FC metrics.

2.1 Simulation Analysis

Studies in photon migration in tissues have shown that photons follow a somewhat banana shape trajectory between a source and detector pair. Placing the source–detector with a certain distance apart, we can probe the tissues with a particular depth sensitivity profile similar to a banana shape, as shown as in Fig. 1.

A signal received by a photodiode includes the changes in the absorption within the underlying tissues. In the near-infrared light spectrum, the highest absorbers are the [Hb] and [HbO]
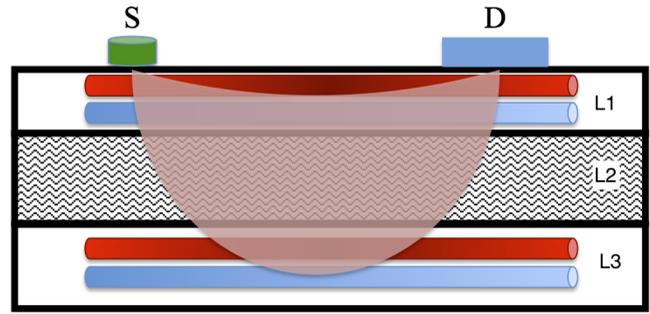

Fig. 1 Geometry of the simulation set up. S, source; D, detector; L1 stands for the skin layer of the head; L2 for skull and cerebrospinal fluid (CSF); and L3 for cortex. Vasculature in L2 has been ignored since it contains negligible amounts of [Hb] and [HbO] variations. The tubes represent the veins running parallel to the source–detector axis. Optical path is illustrated as the semitransparent banana shaped figure.

and a spectroscopic measurement of the absorption will yield the concentration changes of these chromophores, which can be calculated from Beer–Lambert's law, explained in detail in other studies.[1,35–37] Since absorption change within a layer of tissue l at a specific wavelength λ is formulated as $\Delta\mu_l^\lambda = \varepsilon_C^\lambda \Delta \mathbf{C}_l$, where $\varepsilon_C^\lambda = [\varepsilon_{Hb}^\lambda \varepsilon_{HbO}^\lambda]$ and $\Delta \mathbf{C}_l = (\Delta[Hb]_l \Delta[HbO]_l)^T$ for fNIRS studies, we can define a signal model for the [Hb] and [HbO] concentrations for any l layer in the form of Hb_l and HbO_l.

2.1.1 Signal model

Let us assume that the hemodynamic changes $[h_l^C(t)]$ at each layer (l) for given chromophore (C) can be modeled as a sum of independent signal activity ($\mathbf{S}$) weighted with layer specific weights ($\mathbf{W}$), as shown below:

$$h_l^C(t) = \mathbf{WS}, \tag{5}$$

where the entries of the matrix $\mathbf{W}$, $w_{l,k}$ are the weights of a specific hemodynamic activity $s_k(t)$ at that specific layer l that are the entries of the $\mathbf{S}$ matrix. For the sake of simplicity, we will assign three signal activities to be present at each layer: $s^b(t)$, brain hemodynamic response function (BRHF); $s^s(t)$, task irrelevant systemic physiological hemodynamic fluctuations; and $s_n(t)$, uncorrelated instrumentation noise, modeled as $\mathcal{N}(0, \sigma_n)$. Hence, $\mathbf{S} = [s^b(t) s^s(t) s_n(t)]$. Naturally, the weight of $s^b(t)$ for the first and second layers will be zero (i.e., $w_1^b = w_2^b = 0$, $w_3^b = 1$) while $0.1 \leq w_1^s = w_2^s = w_3^s \leq 1$.

Traditionally, $s^b(t)$ and $s^s(t)$ are defined as follows:

$$s^b(t - \theta_i^b) = (t - \theta_i^b)^2 e^{-\left[\frac{(t-\theta_i^b)}{\tau}\right]}, \tag{6}$$

$$s^s(t - \theta_i^s) = \left\{ \sin\left[2\pi \frac{f_1}{f_s}(t - \theta_i^s)\right] + \sin\left[2\pi \frac{f_2}{f_s}(t - \theta_i^s)\right] \right\}, \tag{7}$$

where $s^b(t - \theta_i^b)$ is the brain BHRF modeled as a gamma function with a delay of θ_i^b, a linearly increasing value for each channel ranging from 3 to 10 s to assure a variance in the correlation values between each channel;[38,39] $s^s(t - \theta_i^s)$ is the systemic
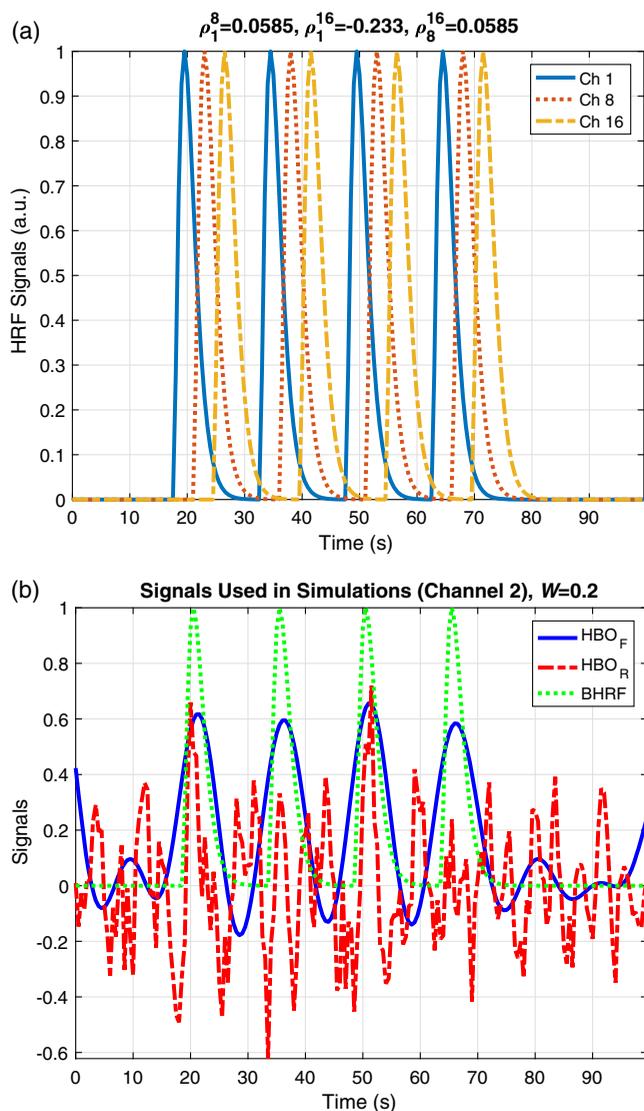
(a)

(b)

Fig. 2 (a) Simulated HRF signals for different channels with a certain delay. (b) A mixed signal simulation for channel 1 based on Eq. (5) with $s^b(t)$ in green, the mixed signal $h_l(t)$ in blue, and subtracted filtered signal $\hat{x}(t)$ in red. The parameters of the simulation are $w_3^b = 1$, $\tau = 1$, $w_3^s = 0.1$, $f_1 = 0.1$ Hz, $f_2 = 0.25$ Hz, $f_s = 2$ Hz, and $s_n(t) = \mathcal{N}(0, 0.01)$.

fluctuations, typically, the Mayer's wave (resonance frequency of f_1) and the breathing-related hemodynamic fluctuations (resonance frequency of f_2), with a randomized delay of θ_i^s for each channel and f_s is the sampling rate. Simulated signals for several channels and the correlation between them can be seen in Fig. 2(a). Figure 2(b) shows the original BHRF and the mixture signal from Eq. (5).

In all the simulations, $w_3^b = 1$ while $w_1^s = w_2^s = w_3^s$ and $w_3^s = \{0.1, 0.2, \ldots, 1\}$.

2.1.2 Functional connectivity analysis

We have decided to use a rectangular probe geometry to simulate the fNIRS signals, as shown in Fig. 3.

We decided to compute the FC using a PC-based analysis. PC provides a relationship between two variables after removing the overlap from both variables. The diagram in Fig. 4 depicts
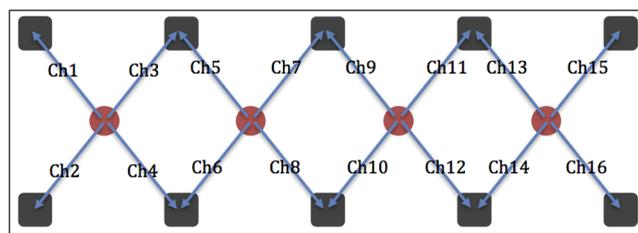

Fig. 3 Rectangular probe geometry used in the simulations. The sources are the red circles while the detectors are the black squares. The source–detector separation is fixed at 2.5 cm. Probe is placed so that channel 1 is on the left, midline of the probe is aligned with the midline of the forehead, and the bottom row is right above the eyebrows. A detailed placement and anatomic localization of the probe can be seen in Ref. 4.
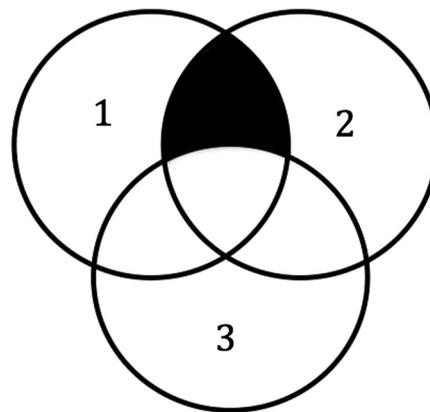

Fig. 4 The shaded region is a graphical representation of the PC between 1 and 2 in the presence of 3.

PC between time series 1 and 2 in the presence of a third time series 3. The PC coefficient between 1 and 2 after removing the influence of 3 ($r_{1,2|3}$) is as follows:[20]

$$r_{1,2|3} = \frac{r_{1,2} - r_{1,3}r_{2,3}}{\sqrt{(1 - r_{1,3}^2)}\sqrt{(1 - r_{2,3}^2)}}. \tag{8}$$

This equation can be generalized to compute PC between any two channels (i, j) as $r_{i,j|k}$ in the presence of a common influencer (k).

Since the fNIRS signal model assumes a linear addition of the BHRF with systemic fluctuations and noise, we assumed a certain frequency band for the brain-related signals and systemic fluctuations.

2.2 fNIRS Data

The data were collected in an earlier study.[24,40] Twelve healthy controlled subjects performed the computerized version of the color-word matching Stroop task.[41] The subjects were asked to respond to 90 stimuli presented on a screen every 4 s, in groups of six stimuli within each block. Fifteen blocks were divided into five NS, five CS, and five IcS type of stimuli and presented in a random fashion. There were 20 s of rest within each block. The subjects were asked to respond to stimuli by pressing either the left or the right button of the mouse based on a match or unmatch condition. fNIRS data were collected with a 16 channel dual wavelength continuous wave system with a sampling rate

of 1.7 Hz (ARGES Cerebro, Hemosoft Inc., Ankara, Turkey). The source–detector configuration is shown in Fig. 3 with a separation of 2.5 cm. Absorption data collected at each detector are converted to [Hb] and [HbO] via the modified Beer–Lambert's Law. The protocol was approved by the Ethical Review Committee of Bogazici University.

2.2.1 Functional connectivity analysis

Both the [Hb] and [HbO] data from each channel are passed through a high pass filter (Butterworth, eigth order, $f_c = 0.09$ Hz) to obtain the HBO_R^i and HB_R^i. The regressor used in PC-based FC analysis is obtained by averaging this signal over all the channels. Hence, $\overline{HBO}_R = \sum_i HBO_R^i$ ($\overline{HB}_R = \sum_i HB_R^i$) is used to regress out the systemic physiological effects from the correlation of the unprocessed [HbO] ([Hb]) signals from two channels. Once the regressor is computed, NS, CS, and IcS parts are consolidated to form individual time series for these stimuli. The FC matrices computed for individual time series are thus termed as $\mathcal{FC}_N$, $\mathcal{FC}_C$, and $\mathcal{FC}_I$.

2.2.2 Global efficiency

One of the aims of cognitive neuroscience is to investigate the neural correlates of cognition.[42–44] Graph-based network analysis is the state-of-the-art methodology in brain connectivity. We considered the channels as a set of vertices V and the PC coefficients as assigned weights on the set of edges E, between vertices to construct an undirected complete weighted graph $G = (V, E)$.[45–47] We investigated the FC graphs of the PCs of each channel for each stimulus type.

Global efficiency (GE) can be evaluated for a wide range of networks, including weighted graphs.[46] Maximal possible GE occurs when all edges are present in the network. The GE value was computed by using the formulation of Latora and Marchiori,[48] since it applies to work with weighted connectivity graphs. In this case, the GE is

$$GE = \frac{1}{N(N-1)} \sum_{i \neq j \in G} \frac{1}{d_{ij}}, \quad (9)$$

where d_{ij} is defined as the smallest sum of the physical distances throughout all the possible paths in the graph from i to j.[48] For weighted graphs, stronger connection weights correspond to shorter lengths. Equation (9) generates values of GE in the range of [0,1].

3 Results

3.1 Simulation Analysis

The simulated signals for various weights as in Eq. (5) were used to compute the FC matrices. The plots in Fig. 5(a) show a sample of such signals while the errors in estimating the FC matrices are given in Fig. 5(b).

The top plot in Fig. 5(a) depicts how difficult it is to observe the presence of the hemodynamic response from the raw [HbO] signal. Figure 5(b) shows how well the PC-based computation of the correlations is closer to real correlation values. As the weight of the systemic fluctuations increases and starts to dominate the whole signal, the accuracy of extracting the real correlation value decreases.
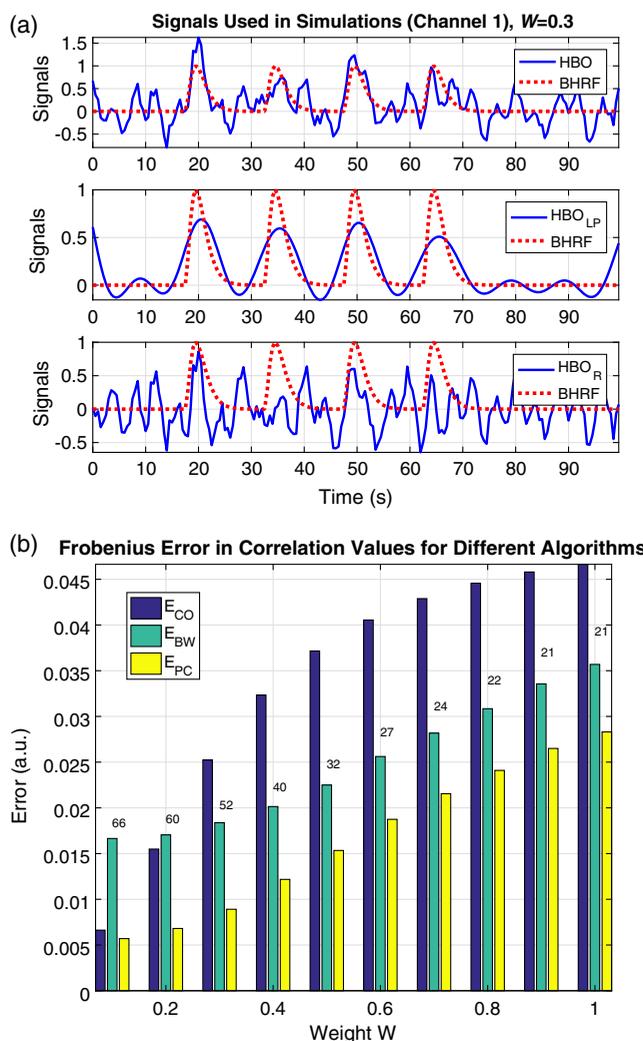

Fig. 5 (a) Simulated HRF signals for different channels with a certain delay. A mixed signal simulation for channel 1 based on Eq. (5) with $s^b(t)$ in red and the mixed signal $h_l(t)$ in blue. The parameters of the simulation are $w_s = 0.3$, $\tau = 1$, $f_1 = 0.1$ Hz, $f_2 = 0.25$ Hz, $f_s = 2$ Hz, and $s_n(t) = \mathcal{N}(0, 0.03)$. The first plot in (a) shows the raw HbO signal, second row Butterworth low pass filtered signals and last plot shows the averaged regressor signal HbO_R after being passed through a Butterworth type high pass filter, (b) errors in estimating the FC matrices. E_{CO} is the error with respect to Pearson's correlation coefficient, E_{BW} is the error after low pass filtering with a Butterworth filter, and E_{PC} is the error with respect to PC analysis. The numbers above the bars indicate the percent improvement in the accuracy (decrease in the errors) between the low pass filtered and PC-based connectivity matrices.

3.2 Real Data Analysis

A sample of fNIRS data from subject 1 and the corresponding regressor signal ($\overline{HBO}_R$) can be seen in Figs. 6(a) and 6(b). The high pass filter setting was set at 0.09 Hz.[49–51] Once the regressor is obtained, the data are segmented into NS, CS, and IcS parts. The choice of these cutoff frequencies was based on the fact that Mayer's wave is centered around 0.1 Hz with a slight variation from 0.09 to 0.11 Hz.[52–55] So the choice for the cutoff frequency for the high pass filter was based on the lower end of the Mayer's wave band. Note that no further filtering was applied to the raw data when computing the PCs. Once
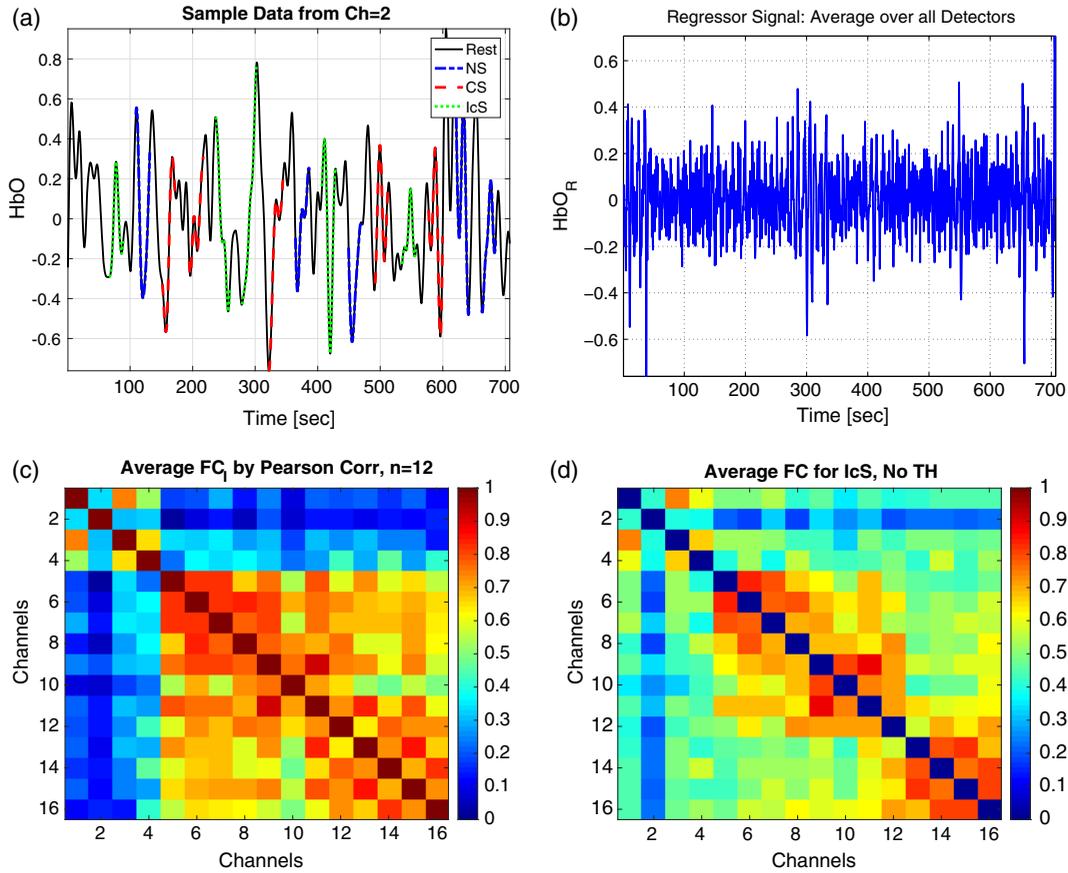
Fig. 6 (a) A representative HBO_2 data from channel 4 of subject 1 is low pass filtered with a fourth order Butterworth filter with a cutoff frequency at 0.08 Hz.[49] NS, CS, and IcS episodes are marked with varying colors. (b) The regressor for subject one is obtained by averaging the high pass filtered signal at 0.09 Hz of each channel. (c) Average of $\mathcal{FC}$ matrices for IcS calculated with Pearson's correlation to low pass filtered data ($n = 12$ subjects, $\overline{\mathcal{FC}_\mathcal{I}}$) and (d) $\overline{\mathcal{FC}_\mathcal{I}}$ matrix calculated by PC.

the regressor is formed from the raw data, then this regressor was used in computing the PC pairs of channels of unfiltered fNIRS data. This way any smearing effect of the spikey artifacts due to low pass filtering was minimized.

3.2.1 *Functional connectivity of real data*

A comparison was made between the conventional FC method and the PC-based FC method. Conventional FC matrices were formed by computing the Person's correlation coefficient of pairs of channels after each fNIRS channel was low pass filtered (in this case with a fourth order Butterworth low pass filter with a cutoff frequency of 0.08 Hz).[49–51] Figures 6(c) and 6(d) show the average of FC matrices for IcS computed by the Pearson's correlation and PC analysis, respectively.

Note that there are high correlations (over 0.8) in almost all the channel pairs for the Pearson's coeffecients [Fig. 6(c)] but not that diffusely scattered for the PC matrix [Fig. 6(d)]. This can be attributed to the fact that there are underlying systemic fluctuations embedded in each channel that dominate the overall correlation between two channels as hypothesized by the signal model in Sec. 2.1.1. This dominance seems to be cleared away in the FC matrix computed via the PC method, as shown in Fig. 6(c). Table 1 compares numerically the FC matrices for three different stimuli computed by the Pearson's correlation,

Table 1 Average of FC matrices $\{\sum_{i=1}^{16} \sum_{j=1}^{16} [\mathcal{FC}_\mathcal{I}(i,j) - \mathcal{FC}_\mathcal{N}(i,j)]\}$ computed over 12 subjects with different algorithms. TH-partial: thresholded PC matrices.

ST	Pearson's correlation	Partial	TH-partial
NS	0.5042	0.4110	0.0729
CS	0.5153	0.3517	0.0714
ICS	0.5285	0.4031	0.0718

PC, and thresholded PC approach in which the common regressor $\overline{HBO_R^S}$ (S is NS, CS, or IcS) is used.

These results elucidate the fact that there is a strong dominance of the background activity present in the signals that represents itself as high correlations among channels. This strong dominance of the underlying background activity is also evident by the fact that as the stimulus gets more demanding, the average strength of correlation increases in Pearson's coefficients but not in PC coefficients. This increase can be explained by a stimulation of the sympathetic system during activities demanding higher cognitive engagement that leads to an increase of heart rate, blood pressure, blood flow to the brain, and breathing rate. On the contrary, no significant increase

is observed for the values obtained by the PC analysis (see second column of Table 1). The elimination of this dominance is also evident in the decrease of the average strength of the correlations, as shown in the last row of Table 1 (from 0.5285 to 0.4031, a 23% decrease).

3.2.2 GE values for real data

The FC matrices are usually thresholded at a certain cutoff level to leave only a percent of the strongest connections before the computation of GE values. A scan of threshold values leaving the strongest 15 to 25 values yielded the highest significance among three different stimuli at GE values for [HbO] FC matrices (TH = 21) and TH = 24 for [Hb]. Average of the thresholded [HbO] FC matrices computed after thresholding at these values is shown in Figs. 7(a)–7(d), while their average correlation values are shown in the last column of Table 1. The average of the interference matrices ($\overline{\mathcal{FC}_\mathcal{I} - \mathcal{FC}_\mathcal{N}}$) in Fig. 7(d) shows an increase of the correlation values in the right dorsolateral prefrontal cortex (dlPFC), which is in line with several of the fNIRS findings.

Since not every subject had high correlations for the same channel pairs, the average values are lower for the averaged FC matrices [note the highest value in the colorbar is 0.6 for Figs. 7(a)–7(c)]. The average of thresholded FC matrices shows a clustering trend toward the right dlPFC (channels 9 to 16) as the stimulus became cognitively more demanding. Figure 7(d) is the difference between Figs. 7(a) and 7(c), and elucidates that

the correlation values on the right dlPFC increases in strength (an average increase of 0.0028) while a consecutive decrease (an average of −0.0056) is observed for the left dlPFC (channels 1 to 8).

The GE values computed from the FC matrices generated by regular correlation (Pearson's correlation coefficient) of low pass filtered data (via Butterworth filter) did not show any significant differences for various types of stimuli ($p > 0.05$). When the correlations are computed via the PC analysis, we observed an increase in the GE values as the cognitive task became more demanding. GE values apparently change with respect to the threshold used for the FC matrices. We swept the threshold values (TH) and observed the significance among the GE_N, GE_C, and GE_{Ic} both for [Hb] and [HbO] values. The TH value shows that the highest significance was observed for TH = 21 for [HbO], which corresponds to 8.75% of the highest correlations when the diagonals are omitted (21/240) and TH = 24 for [Hb] data. In a study by Zhang et al.,[30] a strong lateralization effect was observed, favoring the flow of information to the right side. We grouped the detectors into four areas, where L (left) corresponds to the GE computed for detectors from the FC matrices 1 through 8 [$i = 1...8$, $j = 1...8$ in Eq. (9)], R (right) for detectors from 9 through 16 [$i = 9...16$, $j = 9...16$ in Eq. (9)], IH corresponds to interhemispheric connectivity and the GE was computed from FC matrices of 1 through 8 with 9 through 16th detectors [$i = 1...8$, $j = 9...16$ in Eq. (9)], as shown with dark squares in Fig. 7(d). Whole (W) corresponds to the GE computed from the full FC
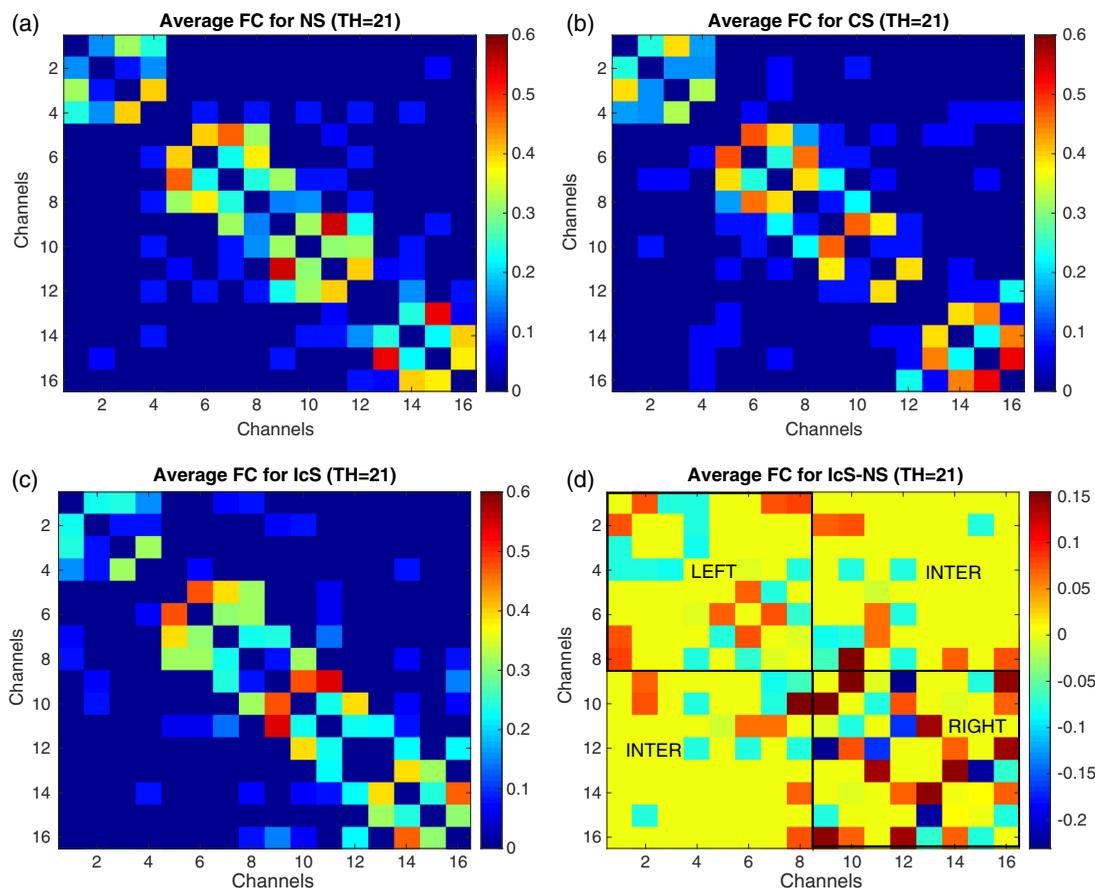

Fig. 7 Average of FC matrices over all subjects for (a) NS, (b) CS, (c) IcS, and (d) interference for IcS-NS are shown. Note that the interference values are in the range of −0.2 to 0.2.

Table 2 GE values (rounded) with respect to PFC areas for the three stimuli types. Standard deviations are discarded but statistical significance (p value) was computed by paired two-tailed t-test. n is the number of subjects included in this analysis.

	Hb ($n = 6$, TH $= 24$)				HbO ($n = 10$, TH $= 21$)			
ST	L$^+$	R	IH*	W*	L$^+$	R*	IH	W*
N	0.57	0.51	0.43	0.12	0.51	0.48	0.34	0.10
C	0.53	0.52	0.42	0.12	0.49	0.46	0.36	0.11
IC	0.52	0.55	0.47	0.14	0.46	0.56	0.36	0.13

Note: ST, stimulus type. $^+$ indicates $p < 0.1$, while * indicates $p < 0.05$.

matrix. Table 2 shows the change of GE with respect to different stimuli for different areas of the PFC. As the GE in the left both for [Hb] and [HbO] decreases with varying stimuli difficulty in a statistically nonsignificant manner, the GE in the right both for
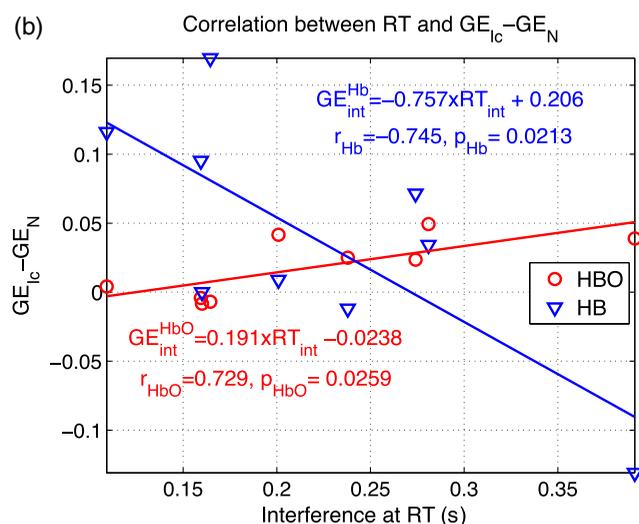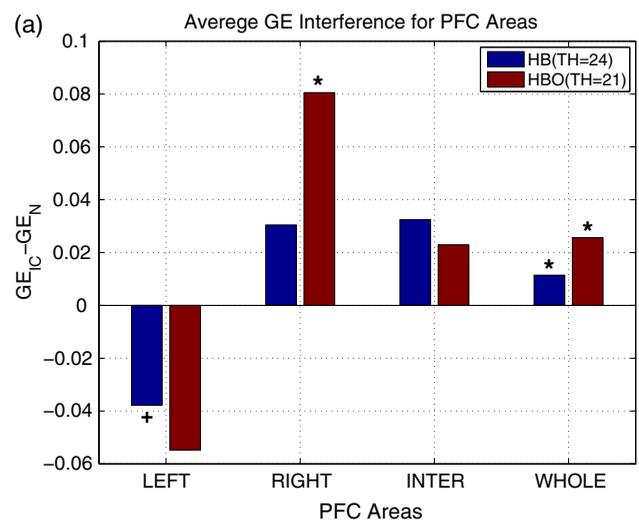

(a)

(b)

Fig. 8 (a) Average interference of GE (GE$_{IC}$ − GE$_N$) from [Hb] ($n = 6$) and [HbO] ($n = 10$) data for the different areas of PFC (+ for $p < 0.1$, * for $p < 0.05$). (b) Correlation with the interference of the behavioral data (reaction rates RT_{Ic} − RT_N) with interference of GE (GE$_{Ic}$ − GE$_N$) for the whole PFC.

[Hb] and [HbO] shows a statistically significant increase. This finding is consistent with the literature where the Stroop interference affect was found to be localized bilaterally.[30,40,41,56,57] Zhang et al.[30] claim to see an increase in the information flow from left to right dlPFC during interference. Figure 7(d) and consecutively Table 2 lead us to speculate that connectivity strength increases in the left and right dlPFC, but the connectivity pattern is diffused in the left while being more focused for the right.

It should be mentioned that the number of subjects included in the analysis in Table 2 had to be trimmed to achieve statistical significance. Only the highest and lowest GE values obtained from [HbO] data are eliminated while a higher number of subjects had to be eliminated from [Hb] data to achieve same significance levels. This result is in line with the literature, where [HbO] data are favored over [Hb] in cognitive studies due to its higher sensitivity to cognition-related hemodynamic changes.

The average interference values computed from GE for [Hb] and [HbO] data are shown in Fig. 8(a). Interference of the behavioral data (as reaction rates) shows a positive (negative) correlation for the interference values of the [HbO] ([Hb]) data, as shown in Fig. 8(b).

4 Discussion

Systemic physiological fluctuations have a deteriorating effect on the accuracy of computing the correlation of fNIRS signals.[29,58–61] Several studies have attempted to address this issue by either advanced signal processing techniques or improvements in instrumentation and probe design albeit at increased cost and complexity of engineering.[2,62]

The current study proposes the use of PC-based connectivity computation under the assumption that a far detector signal is contaminated with systemic fluctuations that cannot be separated or regressed out with advanced signal processing techniques due to overlaps in time and frequency domains. Hence, the only solution becomes a statistical means of computing the correlation between a pair of channels.

4.1 On the Accuracy of Low Pass Filtering

We have shown in the first two scenarios that filtering with a low pass filter does not improve the correlation estimation since we do not have access to the frequency characteristics of the systemic fluctuations. The shortcoming of a correlation computation after signals is low pass filtered, which can be proven by deductive reasoning as follows.

Assume that the i'th detector signal [$x_i(t)$] is modeled as the sum of the brain activity, $s_i^b(t)$, and nuisance term, $s^n(t)$, [$x_i(t) = s_i^b(t) + s^n(t)$] and j'th detector signal as [$x_j(t) = s_j^b(t) + s^n(t)$]. Assuming that there is an overlap in the spectrum
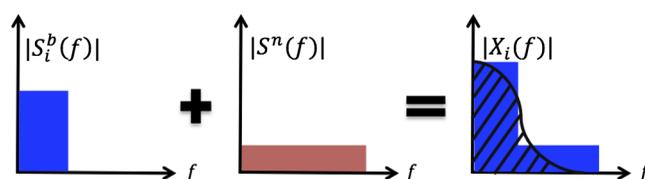

Fig. 9 Spectral composition of the signal from the i'th detector, $|X_i(f)|$, can be given as the sum of the spectrum of the band-limited brain signal, $|S_i^b(f)|$, with the spectrum of the wide-band nuisance signal, $|S^n(f)|$, which is the sum of systemic fluctuations and other types of noises. Typical filter response is superimposed on the last graph.

of these signals, as depicted in Fig. 9, then a low pass filter applied to the sum signal (spectrum with $|X_i(f)|$) will inevitably include a piece of the nuisance spectrum.

Since low pass filters have nonideal characteristics, a leakage of unwanted signals will be present in the filtered signal. This will result in inaccurate estimation of the correlation coefficient. This same problem of a background activity dominating the channels exists in EEG analysis, where due to volume conduction effect, channels are superimposed with this background activity. This must be removed if accurate correlations are to be computed. Our results show a deviation from the original connectivity values even after signals are filtered with various filter types. Error in FC matrices for the Butterworth type of filter produces very similar yet lower error values compared to no preprocessed data, as expected. As the contamination weight increases (i.e., increase in w_i^s) so do the errors in computing the correlation values, as shown in Fig. 5(b).

4.2 On the Accuracy of PC-based Approach

Since there is some sort of dependence between the brain signals and the contaminating signals both in the time and frequency domains, it would be extremely difficult to try to separate them from each other with conventional signal processing tools, such as digital filtering, PCA, or ICA. All these methods require several conditions of independence in time or frequency domain. Kalman filtering would work if there were access to systemic fluctuation data with a detector placed closer to the source (short detector), as has been proposed by several investigators.[6,13,63–66] Hence, the only solution if one wants to compute the correlation under such dependence assumption and a fixed source–detector separation is the use of a PC approach, where one can compute the correlation under a controlled variable. This is exactly what the simulation shows. Its accuracy exceeds by far both the filtered scenarios by almost two to three folds, as shown in Fig. 5(b). Yet even this approach cannot reach a zero level accuracy due to its use of a filter (this time a high pass filter used when computing the nuisance signal that will be used as the controlling variable). Hence, the success of this method depends on how good the nuisance signal can be provided to the algorithm. One solution is the use of a short detector, which will pick up signals only from the skin. Similarly, the use of a pulse oximetry signal even from the fingertip might prove to be useful as long as one can account for the delays in the systemic activity. Similar to the low pass filter's performance, the PC-based approach starts to fail as the contamination level increases.

One alternative approach could be the use of this common nuisance signal (HBO_R) in regressing it from the main detector signal using a general linear model (GLM) based approach. This might be possible but it will introduce other computational steps before actually computing the correlation (first the GLM approach, then reconstruct the HBO signal with the β's that are statistically inferred from the GLM approach, then compute the correlation). Hence, it will undoubtedly introduce more errors even due to the use of numerical methods.

4.3 Real Data Analysis

Having shown that if one has access to only far detector data and no means to measure some sort of systemic activity, then PC-based connectivity analysis is the best choice. Our results show that with conventional means of computing, the connectivity

yielded statistically nonsignificant findings in our fNIRS connectivity analysis. A very significant difference is observed among the GE for the three different stimulus types, as shown in Table 2. Several studies have shown a right dominance for the Stroop activity.[30] Our results also confirm a shift toward right dlPFC connectivity as the stimulus becomes more challenging [from neutral stimulus (NS) to incongruent stimulus (IcS)], as shown in Table 2. As the GE in the left PFC decreases for increasing task complexity, the right PFC picks up and the interhemispheric GE increases, as shown in Fig. 8(a) although not significantly. There is a clear dominance of the left dlPFC, as indicated by many activation and connectivity studies.[40,67–74] Astolfi et al.[75] showed a bilateral connectivity in the Stroop task with a "predominance of outflow from right premotor and prefrontal cortical areas." In both the [Hb] and [HbO] GE results, we see a drop in the incongruent stimuli compared to the neutral stimuli in the left side and a consequent increase in the interhemispheric and whole head interference results [Fig. 8(a)]. This can be interpreted as the aggregation of shorter paths to one longer path (leading to an increase in GE) for the [HbO] signal.

Similar to some fMRI studies, there is a negative correlation between the interference observed in reaction rates and the interference computed by GE values, as shown in Fig. 8(b), for [HbO] at the left and interhemispheric connectivity metrics. A significant positive correlation is observed for the [HbO] for whole head connectivity analysis ($r = 0.729$, $p = 0.0259$) while a significant negative correlation ($r = -0.745$, $p = 0.0213$) is observed for interhemispheric connectivity from [Hb] data, as shown in Fig. 8(b). A positive correlation between the interference computed for the reaction rates and GE values means that as the cognitive challenge increases, sequential short paths are replaced by one long path, a direct connection between distant areas. An exact opposite is observed for the [Hb] interference, where the negative correlation means that a smaller interference in reaction times gives higher interference in GE values. An explanation can be as follows: as the cognitive challenge increases, brain regions working in coherence increase, leading to a simultaneous demand of oxygenated blood to those regions (hence an increase in the GE observed for [HbO]), yet the venous side is not necessarily as coordinated leading to a drop of efficiency. Neurovascular coupling literature has united on the finding that both neurons and astrocytes may lead to a vasodilation of the arteriole smooth muscle cells in response to glutamate releases during neuronal activation.[76,77] We might also infer that [Hb] activity is mostly regulated on a regional basis in a passive way and independent of the unification required for responding to a cognitive challenge, much similar to a balloon effect.[78–80] That type of demand can be explained only by the increase in [HbO] activation and its GE metrics.

5 Conclusions

This study aimed at proposing a PC-based FC analysis for fNIRS [HbO] and [Hb] signals collected during a color word matching Stroop task. GE values calculated from the connectivity metrics of [HbO] signals reveal that as the cognitive challenge increases, so does the GE value. The use of PC-based analysis was preferred since the optode signals suffer greatly from systemic physiological interference. We proposed a method to eliminate its biasing effect when a correlation is computed between a pair of channels. This way the reliability of the

connectivity analysis is improved and the results are consequently more accurate.

Disclosures

There are no conflicts of interest to disclose.

References

1. B. Chance, "Optical method," *Ann. Rev. Biophys. Biophys. Chem.* **20**, 1–30 (1991).
2. T. Funane et al., "Quantitative evaluation of deep and shallow tissue layers' contribution to fNIRS signal using multi-distance optodes and independent component analysis," *Neuroimage* **85**(1), 150–165 (2014).
3. D. A. Boas, A. M. Dale, and M. A. Franceschini, "Diffuse optical imaging of brain activation: approaches to optimizing image sensitivity, resolution, and accuracy," *Neuroimage* **23**(Suppl. 1), S275–S288 (2004).
4. S. B. Erdoĝan, M. A. Yücel, and A. Akın, "Analysis of task-evoked systemic interference in fNIRS measurements: insights from fMRI," *Neuroimage* **87**, 490–504 (2014).
5. M. A. Franceschini et al., "Hemodynamic evoked response of the sensorimotor cortex measured noninvasively with near-infrared optical imaging," *Psychophysiology* **40**(4), 548–560 (2003).
6. L. Gagnon et al., "Short separation channel location impacts the performance of short channel regression in NIRS," *Neuroimage* **59**(3), 2518–2528 (2012).
7. E. Kirilina et al., "The physiological origin of task-evoked systemic artefacts in functional near infrared spectroscopy," *Neuroimage* **61**(1), 70–81 (2012).
8. I. Tachtsidis et al., "False positives in functional near-infrared topography," *Adv. Exp. Med. Biol.* **645**, 307–314 (2009).
9. S. Tak and J. C. Ye, "Statistical analysis of fNIRS data: a comprehensive review," *Neuroimage* **85**(1), 72–91 (2014).
10. Q. Zhang, E. N. Brown, and G. E. Strangman, "Adaptive filtering for global interference cancellation and real-time recovery of evoked brain activity: a Monte Carlo simulation study," *J. Biomed. Opt.* **12**(4), 044014 (2007).
11. S. Brigadoi and R. J. Cooper, "How short is short? Optimum source-detector distance for short-separation channels in functional near-infrared spectroscopy," *Neurophotonics* **2**(2), 025005 (2015).
12. J. R. Goodwin, C. R. Gaudet, and A. J. Berger, "Short-channel functional near-infrared spectroscopy regressions improve when source-detector separation is reduced," *Neurophotonics* **1**(1), 015002 (2014).
13. L. Gagnon et al., "Further improvement in reducing superficial contamination in NIRS using double short separation measurements," *Neuroimage* **85**(1), 127–135 (2014).
14. T. Yamada, S. Umeyama, and M. Ohashi, "Removal of motion artifacts originating from optode fluctuations during functional near-infrared spectroscopy measurements," *Biomed. Opt. Express* **6**(12), 4632–4649 (2015).
15. Y. Zhang et al., "Multiregional functional near-infrared spectroscopy reveals globally symmetrical and frequency-specific patterns of superficial interference," *Biomed. Opt. Express* **6**(8), 2786–2802 (2015).
16. T. Chen et al., "Estimation of resting-state functional connectivity using random subspace based partial correlation: a novel method for reducing global artifacts," *Neuroimage* **82**(0), 87–100 (2013).
17. Z. Einalou et al., "Functional near infrared spectroscopy to investigation of functional connectivity in schizophrenia using partial correlation," *Univ. J. Biomed. Eng.* **2**(1), 5–8 (2014).
18. P. Fransson and G. Marrelec, "The precuneus/posterior cingulate cortex plays a pivotal role in the default mode network: evidence from a partial correlation network analysis," *Neuroimage* **42**(3), 1178–1184 (2008).
19. G. Marrelec et al., "Using partial correlation to enhance structural equation modeling of functional MRI data," *Magn. Reson. Imaging* **25**(8), 1181–1189 (2007).
20. G. Marrelec et al., "Partial correlation for functional brain interactivity investigation in functional MRI," *Neuroimage* **32**(1), 228–237 (2006).
21. S. Ryali et al., "Estimation of functional connectivity in fMRI data using stability selection-based sparse partial correlation with elastic net penalty," *Neuroimage* **59**(4), 3852–3861 (2012).
22. F. T. Sun, L. M. Miller, and M. D'Esposito, "Measuring interregional functional connectivity using coherence and partial coherence analyses of fMRI data," *Neuroimage* **21**(2), 647–658 (2004).
23. J. Shi et al., "Correlation between LIFG and autonomic activation during stressful tasks: a functional near-infrared spectroscopy (fNIRS) study," *J. Huazhong Univ. Sci. Technol. Med. Sci.* **34**(5), 663–671 (2014).
24. S. Aydore et al., "On temporal connectivity of PFC via Gauss-Markov modeling of fNIRS signals," *IEEE Trans. Biomed. Eng.* **57**(3), 761–768 (2010).
25. U. Lindauer et al., "Pathophysiological interference with neurovascular coupling–when imaging based on hemoglobin might go blind," *Front. Neuroenerg.* **2**, 25 (2010).
26. R. C. Mesquita, M. A. Franceschini, and D. A. Boas, "Resting state functional connectivity of the whole head with near-infrared spectroscopy," *Biomed. Opt. Express* **1**(1), 324–336 (2010).
27. H. Niu et al., "Test-retest reliability of graph metrics in functional brain networks: a resting-state fNIRS study," *PLoS One* **8**(9), e72425 (2013).
28. S. Sasai et al., "Frequency-specific functional connectivity in the brain during resting state revealed by NIRS," *Neuroimage* **56**(1), 252–257 (2011).
29. H. Zhang et al., "Functional connectivity as revealed by independent component analysis of resting-state fNIRS measurements," *Neuroimage* **51**(3), 1150–1161 (2010).
30. L. Zhang et al., "Studying hemispheric lateralization during a stroop task through near-infrared spectroscopy-based connectivity," *J. Biomed. Opt.* **19**(5), 057012 (2014).
31. H. Niu and Y. He, "Resting-state functional brain connectivity: lessons from functional near-infrared spectroscopy," *Neuroscientist* **20**(2), 173–188 (2014).
32. J.-H. Wang et al., "Graph theoretical analysis of functional brain networks: test-retest evaluation on short- and long-term resting-state functional MRI data," *PLoS One* **6**(7), e21976 (2011).
33. M. Dadgostar et al., "Functional connectivity of the PFC via partial correlation," *Optik-Int. J. Light Electron Opt.* **127**(11), 4748–4754 (2016).
34. E. Sakakibara et al., "Detection of resting state functional connectivity using partial correlation analysis: a study using multi-distance and whole-head probe near-infrared spectroscopy," *Neuroimage* **142**, 590–601 (2016).
35. D. T. Delpy et al., "Estimation of optical pathlength through tissue from direct time of flight measurements," *Phys. Med. Biol.* **33**, 1433–1442 (1988).
36. Y. Hoshi and M. Tamura, "Detection of dynamic changes in cerebral oxygenation coupled to neuronal function during mental work in man," *Neurosci. Lett.* **150**, 5–8 (1993).
37. A. Villringer and B. Chance, "Non-invasive optical spectroscopy and imaging of human brain function," *Trends Neurosci.* **20**(10), 435–442 (1997).
38. G. K. Aguirre, E. Zarahn, and M. D'esposito, "The variability of human, BOLD hemodynamic responses," *Neuroimage* **8**(4), 360–369 (1998).
39. J. Steffener et al., "Investigating hemodynamic response variability at the group level using basis functions," *Neuroimage* **49**(3), 2113–2122 (2010).
40. K. Ciftçi et al., "Multilevel statistical inference from functional near-infrared spectroscopy data during stroop interference," *IEEE Trans. Biomed. Eng.* **55**(9), 2212–2220 (2008).
41. S. Zysset et al., "Color-word matching stroop task: separating interference and response conflict," *Neuroimage* **13**(1), 29–36 (2001).
42. R. Adolphs, "The social brain: neural basis of social knowledge," *Ann. Rev. Psychol.* **60**, 693–716 (2009).
43. R. Adolphs, "Cognitive neuroscience of human social behaviour," *Nat. Rev. Neurosci.* **4**(3), 165–178 (2003).
44. R. Adolphs, "Investigating the cognitive neuroscience of social behavior," *Neuropsychologia* **41**(2), 119–126 (2003).

45. Y. He and A. Evans, "Graph theoretical modeling of brain connectivity," *Curr. Opin. Neurol.* **23**(4), 341–350 (2010).
46. F. Skidmore et al., "Connectivity brain networks based on wavelet correlation analysis in Parkinson fMRI data," *Neurosci. Lett.* **499**(1), 47–51 (2011).
47. E. Bullmore and O. Sporns, "Complex brain networks: graph theoretical analysis of structural and functional systems," *Nat. Rev. Neurosci.* **10**(3), 186–198 (2009).
48. V. Latora and M. Marchiori, "Efficient behavior of small-world networks," *Phys. Rev. Lett.* **87**(19), 198701 (2001).
49. H. Zhang et al., "Functional connectivity as revealed by independent component analysis of resting-state fNIRS measurements," *Neuroimage* **51**(3), 1150–1161 (2010).
50. B. R. White et al., "Resting-state functional connectivity in the human brain revealed with diffuse optical tomography," *Neuroimage* **47**(1), 148–156 (2009).
51. D. Zhou, W. K. Thompson, and G. Siegle, "MATLAB toolbox for functional connectivity," *Neuroimage* **47**(4), 1590–1607 (2009).
52. A. J. Metz et al., "Physiological effects of continuous colored light exposure on Mayer wave activity in cerebral hemodynamics: a functional near-infrared spectroscopy (fNIRS) study," *Adv. Exp. Med. Biol.* **977**, 277–283 (2017).
53. U. Sliwka et al., "Spontaneous oscillations in cerebral blood flow velocity give evidence of different autonomic dysfunctions in various types of headache," *Headache* **41**(2), 157–163 (2001).
54. C. Haubrich et al., "M-wave analysis and passive tilt in patients with different degrees of carotid artery disease," *Acta Neurol. Scand.* **109**(3), 210–216 (2004).
55. A. Rowley et al., "Synchronization between arterial blood pressure and cerebral oxyhaemoglobin concentration investigated by wavelet cross-correlation," *Physiol. Meas.* **28**(2), 161–173 (2006).
56. S. J. Moser et al., "Right prefrontal brain activation due to stroop interference is altered in attention-deficit hyperactivity disorder-an fNIRS study," *Neuroimage* **47**, S69 (2009).
57. M. L. Schroeter et al., "Prefrontal activation due to stroop interference increases during development–an event-related fNIRS study," *Neuroimage* **23**(4), 1317–1325 (2004).
58. C.-M. Lu et al., "Use of fNIRS to assess resting state functional connectivity," *J. Neurosci. Methods* **186**(2), 242–249 (2010).
59. L. Dommer et al., "Between-brain coherence during joint n-back task performance: a two-person functional near-infrared spectroscopy study," *Behav. Brain Res.* **234**(2), 212–222 (2012).
60. F. A. Fishburn et al., "Sensitivity of fNIRS to cognitive state and load," *Front. Hum. Neurosci.* **8**, 76 (2014).
61. C.-M. Lu et al., "Use of fNIRS to assess resting state functional connectivity," *J. Neurosci. Methods* **186**(2), 242–249 (2010).
62. B. Molavi, J. Gervain, and G. A. Dumont, "Estimating cortical connectivity in functional near infrared spectroscopy using multivariate autoregressive modeling," in *Annual Int. Conf. of the IEEE Engineering in Medicine and Biology Society (EMBC '11)*, pp. 2334–2337 (2011).
63. R. J. Cooper et al., "A systematic comparison of motion artifact correction techniques for functional near-infrared spectroscopy," *Front. Neurosci.* **6**, 147 (2012).
64. A. F. Abdelnour and T. Huppert, "Real-time imaging of human brain function by near-infrared spectroscopy using an adaptive general linear model," *Neuroimage* **46**(1), 133–143 (2009).
65. V. Kolehmainen et al., "State-estimation approach to the nonstationary optical tomography problem," *J. Opt. Soc. Am. A* **20**(5), 876–889 (2003).
66. S. Prince et al., "Time-series estimation of biological factors in optical diffusion tomography," *Phys. Med. Biol.* **48**(11), 1491–1504 (2003).
67. A.-C. Ehlis et al., "Multi-channel near-infrared spectroscopy detects specific inferior-frontal activation during incongruent stroop trials," *Biol. Psychol.* **69**(3), 315–331 (2005).
68. M. T. Banich et al., "fMRI studies of stroop tasks reveal unique roles of anterior and posterior brain systems in attentional selection," *J. Cognit. Neurosci.* **12**, 988–1000 (2000).
69. M. T. Banich et al., "Prefrontal regions play a predominant role in imposing an attentional 'set': evidence from fMRI," *Cognit. Brain Res.* **10**, 1–9 (2000).
70. M. T. Banich et al., "Attentional selection and the processing of task-irrelevant information: insights from fMRI examinations of the stroop task," *Prog. Brain Res.* **134**, 459–470 (2001).
71. S. A. Herd, M. T. Banich, and R. C. O'Reilly, "Neural mechanisms of cognitive control: an integrative model of stroop task performance and fMRI data," *J. Cognit. Neurosci.* **18**, 22–32 (2006).
72. X. Liu et al., "Functional dissociation of attentional selection within PFC: response and non-response related aspects of attentional selection as ascertained by fMRI," *Cereb. Cortex* **16**, 827–834 (2006).
73. R. L. Silton et al., "Depression and anxious apprehension distinguish frontocingulate cortical activity during top-down attentional control," *J. Abnorm. Psychol.* **120**, 272–285 (2011).
74. R. L. Silton et al., "The time course of activity in dorsolateral prefrontal cortex and anterior cingulate cortex during top-down attentional control," *Neuroimage* **50**, 1292–1302 (2010).
75. L. Astolfi et al., "Imaging functional brain connectivity patterns from high-resolution EEG and fMRI via graph theory," *Psychophysiology* **44**(6), 880–893 (2007).
76. D. Attwell and C. Iadecola, "The neural basis of functional brain imaging signals," *Trends Neurosci.* **25**(12), 621–625 (2002).
77. C. Huneau, H. Benali, and H. Chabriat, "Investigating human neurovascular coupling using functional neuroimaging: a critical review of dynamic models," *Front. Neurosci.* **9**, 467 (2015).
78. A. Aubert et al., "Modeling of pathophysiological coupling between brain electrical activation, energy metabolism and hemodynamics: insights for the interpretation of intracerebral tumor imaging," *Acta Biotheor.* **50**(4), 281–295 (2002).
79. R. A. D. Blasi et al., "Noninvasive measurement of human forearm oxygen consumption by near infrared spectroscopy," *Eur. J. Appl. Physiol.* **67**(1), 20–25 (1993).
80. R. B. Buxton et al., "Modeling the hemodynamic response to brain activation," *Neuroimage* **23**(Suppl 1), S220–S233 (2004).

Ata Akın received his PhD in biomedical engineering from Drexel University in 1998. He holds his BS degree in electronics and telecommunications engineering from Istanbul Technical University. He serves as the dean of Faculty of Engineering at Acibadem University, since 2015. His interests are in functional neuroimaging, fNIRS, mathematical physiology, and biodesign.